

Microscopic origin of scalar potential induced topological transition in massive Dirac fermions and scalar Hall effect

Sumit Ghosh^{1,2,3,*}, Yuriy Mokrousov^{2,3} and Stefan Blügel²

¹Max Born Institute for Nonlinear Optics and Short Pulse Spectroscopy, 12489 Berlin, Germany

²Peter Grünberg Institut (PGI-1), Forschungszentrum Jülich GmbH, 52428 Jülich, Germany

³Institute of Physics, Johannes Gutenberg-University Mainz, 55128 Mainz, Germany



(Received 25 May 2022; revised 16 August 2024; accepted 22 August 2024; published 9 September 2024)

We present a systematic study of scalar potential induced topological transition in massive Dirac fermions. We show how a distribution of scalar potential can manipulate the signature of the gap or the *mass*, as well as the dispersion leading to a band inversion. This is mediated by the *Klein tunneling* as well as *inverse Klein tunneling*, which makes it inherently different from the mechanism leading to topological Anderson insulator. In one dimension it can lead to the formation of edge localization. In two dimensions this can give rise to the quantized Hall effect. Unlike conventional Hall effects, this is induced by a scalar interaction and is intrinsic in nature. Therefore, we call it a *scalar Hall effect*. This can facilitate direct manipulation of topological invariants, e.g., the Chern number, as well as the manipulation of the edge states locally in a trivial insulator and thus opens new possibilities for tuning physical observables which originate from the nontrivial topology.

DOI: [10.1103/PhysRevB.110.125117](https://doi.org/10.1103/PhysRevB.110.125117)

I. INTRODUCTION

In recent years *topology* has become a central concept in condensed matter physics [1], while materials with nontrivial topological properties have become a key ingredient in designing next-generation transport and memory devices [2,3]. An immense effort has been directed at discovering suitable materials [4,5] and characterization of their topological classes [6,7]. This highly active research field has brought several new topological phases in the last decade [8,9]. The first topological insulator, namely, the quantum Hall insulator, was discovered under a strong magnetic field [10], which is quite challenging for any practical purpose. In materials with strong spin-orbit coupling (SOC), such as HgTe [11] and Bi₂Se₃ [12], the nontrivial topological features arise from electronic interactions involving orbital and spin degrees of freedom. Such interactions can give rise to different topological phases such as the quantum anomalous Hall insulator [13] and quantum spin Hall insulator [14]. Such phases can host *dissipationless* current [15], which opens immense possibilities in device applications due to their robustness against scattering. Impurity scattering can also contribute to the Hall current [16–18] via mechanisms like side jumps and skew scattering, which is known as the *extrinsic* contribution. This is inherently different from the *intrinsic* contribution arising from the internal characteristics of the systems which is often described in terms of the topology of the system [19]. Several physical observables with a connection to real [20] and reciprocal [21] space topology are known to be enhanced in the presence of scalar impurity, which indicates that the scalar potential might have a deeper connection to the intrinsic

contribution as well. A proper theoretical description of such a connection is still missing.

In certain cases it is possible to tune the topological properties with magnetic impurities [22,23]; however, these cases are very material specific. For most of the cases, SOC is considered to be the source of nontrivial topological properties which manifest via band inversion [24]. The band inversion is, indeed, an impeccable sign of a topological transition; however, on its own, it does not directly reflect the specific mechanism which drives it. In addition, it is also possible to have a topological insulator even without SOC or a magnetic moment [25,26] by exploiting the symmetry of the electronic degrees of freedom. A proper description of the mechanism behind the induced topological features and the transition dynamics between different topological phases is therefore highly desired to access and manipulate the topological phases of solid-state systems.

The key to accessing the nontrivial topological properties of these systems lies in their dispersion, which resembles that of a relativistic particle. One of the characteristic features of relativistic dispersion is that each gap is associated with a well-defined *signature*. For any generic Dirac spinor ψ obeying $(i\gamma^\mu \partial_\mu - m)\psi = 0$ (in natural units $c = \hbar = 1$), where γ^μ ($\mu = 0$ is the temporal component) are the Dirac matrices obeying the Clifford algebra $\{\gamma^\mu, \gamma^\nu\} = 2\eta^{\mu\nu}\mathbb{I}$, with η being the Minkowski metric, the spectrum has a fundamental gap of $2m$. This is commonly known as the *mass gap* since the gap is associated with the rest mass of the particle in relativistic theory. Each energy band is associated with a particular sign of $\langle \gamma^0 \rangle$, and as a result, each gap can be identified with a specific signature. While the eigenvalue spectra remain the same irrespective of the sign of m , the eigenstates are sensitive to it and manifest different topological features. A pronounced example is the appearance of Jackiw-Rabi modes

*Contact author: s.ghosh@fz-juelich.de

at the boundary of two different domains characterized by opposite mass terms [27] where the topological phase boundary is manifested as spatial localization which is the essence of edge states in topological insulators.

To understand the relation between the mass term and topological characteristics of a system, let us consider a generic 2×2 Dirac Hamiltonian $\sigma \cdot \mathbf{n}(\mathbf{R})$ defined on a Bloch sphere, where σ is the vector of Pauli matrices and $\mathbf{n}(\mathbf{R})$ is the unit vector parametrized by \mathbf{R} . In this case, the vector Berry curvature is simply given by \mathbf{n} [28]. In two dimensions, two of the Pauli matrices are coupled with momentum corresponding to the direction of motion, while the third is coupled to the mass term. The Chern number in this case follows the same signature of the out-of-plane component of \mathbf{n} , which is nothing but the mass term. A similar correlation was observed in two-dimensional paramagnetic systems and three-dimensional complex heterostructures as well [29]. In a condensed matter system, the mass term is associated with an order parameter and therefore can be exploited to identify different phases [30]. In a real system, however, manipulating the mass term is quite nontrivial. The mass term does not commute with the rest of the Hamiltonian and thus results in intriguing new topological features [31]. Physically, this noncommuting nature originates from a complex mixture of different degrees of freedom, which makes controlling them quite challenging. A simple way to manipulate the magnitude and signature of the mass gap thus has enormous potential for fabricating topologically nontrivial systems and exploring their applications.

In this work, taking a generic two-band system as a prototype, we present a systematic analysis of the topological properties in a multiband system and demonstrate a simplified way to generate and manipulate nontrivial topological features with the help of the scalar potential. In practice, this scalar potential can be introduced by means of nanopatterning [32] or a surface superlattice [33]. By using the two-band Dirac Hamiltonian, we demonstrate how one can manipulate the mixture of different quantum states, which in turn controls the topological features. Since the scalar potential is represented by an identity matrix which commutes with any other matrix, our formalism is equally applicable to systems where the nontrivial topology arises from spin or orbital degrees of freedom. The formalism is thus applicable to a large class of condensed matter systems, which facilitates a wide range of applications of this generic protocol.

II. DIRAC EQUATION IN ONE DIMENSION

To understand the connection between the scalar potential and the mass term, let us first consider the one-dimensional Dirac equation in the continuum limit. In one dimension, it is sufficient to consider the 2×2 representation of Dirac matrices, which we choose here as the Pauli matrices σ . We define our system with the one-dimensional Dirac Hamiltonian

$$H_1^D = -i\sigma_1 \partial_x + \sigma_3 m + \sigma_0 V(x), \quad (1)$$

where $V(x)$ is a scalar potential and σ_0 is the identity matrix of rank 2. In the absence of the potential term, the energy spectrum consists of two hyperbolic branches ($E = \pm\sqrt{p^2 + m^2}$, where p is the momentum) separated by a gap of $2m$ with

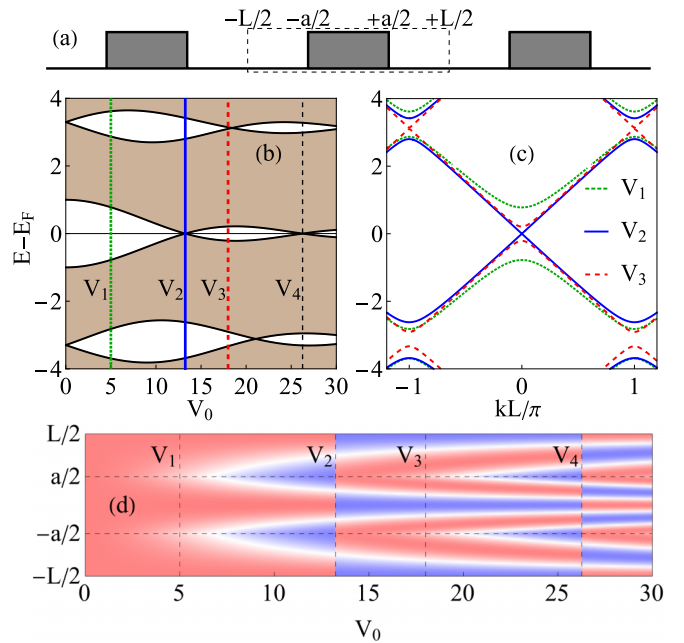


FIG. 1. Variation of mass gap with V_0 . (a) Schematic of the one-dimensional periodic lattice. The dashed box shows the unit cell, and the gray boxes show the scalar potential V_0 . (b) Variation of bandwidth (filled region) with the applied potential. White regions correspond to the band gap. (c) Band structure for selected values of V_0 marked by vertical colored lines in (b). (d) Distribution of the order parameter $\Delta(x)$ over the unit cell with respect to V_0 , where red and blue represent the positive and negative magnitudes, respectively.

positive and negative energy eigenvalues characterized by positive and negative values of $\langle \sigma_3 \rangle$. For such a system, it is possible to achieve complete transmission if the barrier height is greater than twice the mass term ($V_0 > 2m$; Appendix A). This is known as the *Klein paradox* [34], which has attracted a lot of interest in both high-energy physics and condensed matter physics [35]. The simplest way to understand the underlying mechanism is via the mixture of states with positive and negative energies. If the scalar potential is strong enough ($V_0 > 2m$), then it can elevate the negative energy states inside the potential barrier to an energy level occupied by the positive energy states outside the barrier, which creates a continuous channel using plane-wave modes. For a smaller barrier width, interference due to the finite-size effect is more prominent, manifesting as oscillations in transmission probability (Appendix A).

The physics becomes more intriguing if this potential region is employed periodically, which can create states with alternating signs of the mass term in successive regions in space. As a result, although the scalar potential itself cannot alter the mass gap, the interference between states with different mass terms can alter the characteristic band gap. To demonstrate this effect we consider the one-dimensional Dirac-Kronig-Penney model, which has been used to analyze relativistic quarks [36] and fermions [37]. Here we consider a one-dimensional lattice with length L (set to be 1) and with a rectangular potential of height V_0 and width a such that $a/L = 0.4$ and calculate the band structure (Fig. 1). We define

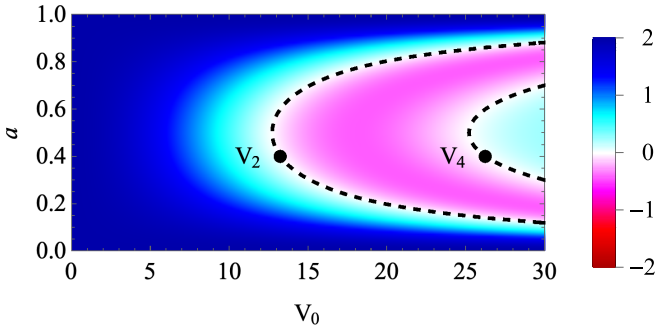


FIG. 2. Variation of the mass gap with the barrier width a and barrier height V_0 . The color shows the value of the mass gap multiplied by the sign of the order parameter at $x = 0$, and the black dashed lines show the transition boundaries for the mass term. V_2 and V_4 show the locations of transition points in Fig. 1.

the spatial order parameter

$$\Delta(x) = [(\langle +, x | \sigma_3 | +, x \rangle - \langle -, x | \sigma_3 | -, x \rangle) / 2]_{k=0}, \quad (2)$$

where $|+, x\rangle$ and $|-, x\rangle$ denote the wave function at x of the lowest positive energy and highest negative energy states. For $V_0 = 0$ these two states reside at energy $E = \pm m$. For $V_0 > 0$, both of these states are shifted by a positive value. To keep these two states symmetric around the zero level we subtract a fixed energy E_F for each value of V_0 . This energy is analogous to the Fermi level in a system with a finite number of states [38].

From Fig. 1 one can see that by increasing the barrier height it is possible to manipulate the mass gap. The mass gap decreases because the potential V_0 now pulls up negative energy states within the window $-m < E < m$ which can now tunnel through the region without potential where the evanescent modes have opposite signatures of the mass term. In a sense, this is the *inverse Klein tunneling*, where the tunneling happens through the potential-free region. This mechanism promotes more mixing of quantum states, which creates a spatial modulation of the order parameter Δ . Note that at some critical values, the gap vanishes completely (V_2, V_4 in Fig. 1), and the distribution of the order parameter also flips sign. This critical potential is minimal when the barrier width is half of the unit cell, which maximizes the mixture of quantum states (Fig. 2). The flipping of the order parameter establishes that each of these crossings is associated with a band inversion. The impact of the band inversion will become more clear when we explore the topological properties of a two-dimensional model in the next section.

III. LATTICE MODEL: FROM ONE TO TWO DIMENSIONS

The transition from the continuum to a lattice model for a relativistic Hamiltonian is not a straightforward task. Since we are not looking into chiral fermions here, we are free from the obstacles imposed by the Nielsen-Ninomiya theorem [39]. For modeling massive/gapped Fermions, one can start from a chiral Fermion and simply add a *mass* term. This produces a pair of fermions with opposite group velocities within the Brillouin zone, commonly known as *doublers*.

To avoid this, one can adopt Wilson's prescription [40] and introduce a momentum-dependent coupling between the spinor components. This is also known as the *Creutz lattice* [41]. For a two-component spinor field $\psi = [a, b]^T$ the Creutz Hamiltonian can be expressed as

$$H_C = iA \sum_j a_{j+1}^\dagger a_j - a_j^\dagger a_{j+1} - b_{j+1}^\dagger b_j + b_j^\dagger b_{j+1} - B \sum_j a_{j+1}^\dagger b_j + b_{j+1}^\dagger a_j + M \sum_j a_j^\dagger b_j + b_j^\dagger a_j. \quad (3)$$

For convenience we perform a unitary transformation $H_1 = U^\dagger H_C U$ [where $U = (\sigma_1 + \sigma_3) / \sqrt{2}$]. The transformed Hamiltonian in reciprocal space is given by $H_1(k) = [M - 2B \cos(k)]\sigma_3 + 2A \sin(k)\sigma_1$. Although the physical outcome does not change under such unitary transformation, the modified form makes it easier to correlate our prediction with known physical systems, which will be clearer when we discuss the scenario in two dimensions.

A. Tuning the topological phase in one dimension:

Emergence of edge localization

We start from the lattice Hamiltonian in one dimension given by

$$H_1(k) = [M - 2B \cos(k)]\sigma_3 + 2A \sin(k)\sigma_1. \quad (4)$$

One can readily see that for $k \rightarrow 0$, the low-energy spectrum corresponds to the continuum Dirac Hamiltonian [Eq. (1)] with a mass gap of $M - 2B$. Here we choose $M = A = 5.0$ and $B = 2.0$ and a unit cell with $L = 40$ sites. A scalar potential of strength V_0 is spanned over a region of $a = 16$ sites. In the absence of any scalar potential, the system has a *mass* $M - 2B = 1$, which is expected in any massive Dirac system. The Fermi level corresponds to half filling and is kept at zero. We define the site-resolved order parameter

$$\Delta_i = [(\langle +, i | \sigma_3 | +, i \rangle - \langle -, i | \sigma_3 | -, i \rangle) / 2]_{k=0}, \quad (5)$$

where $|+, i\rangle$ and $|-, i\rangle$ are the wave functions at site i of the lowest positive energy and highest negative energy states.

From Fig. 3(a), one can readily see that the mass term behaves similar to the continuum model with respect to V_0 . The variation of the band gap in the lattice model [Fig. 3(b)] is also qualitatively the same as the prediction of the continuum model. This establishes the validity of the lattice model for our study. From the band structure, one can see that the distribution of the mass term switches signs as it passes through a band crossing [denoted by vertical black dashed lines in Figs. 3(a) and 3(b)]. To understand whether these jumps are associated with any change in the topological phase, we consider a supercell with 8 unit cells (total 320 sites) and with open boundary conditions. We consider two different strengths of the scalar potential [V_d and V_e in Fig. 3(c)] on either side of the crossing point. One can readily see that after the critical potential, the finite chain has eigenvalues close to zero energy [Fig. 3(c)]. The eigenstates corresponding to these zero-energy modes are strongly localized near the edges [Fig. 3(g)], whereas before the transition the highest occupied and lowest unoccupied states are localized in the bulk [Fig. 3(f)]. One can see that the system

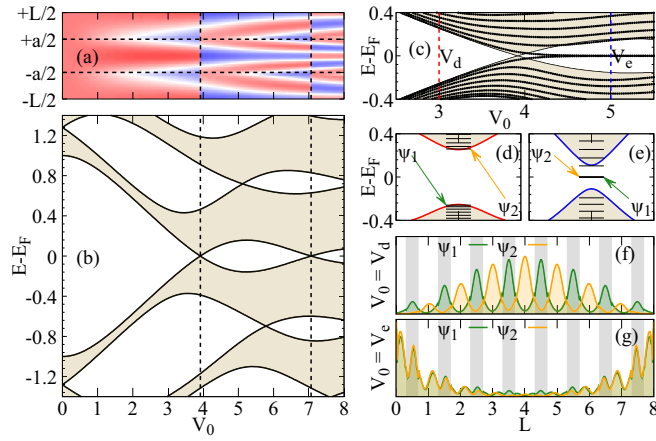


FIG. 3. Tuning the phases of a one-dimensional chain. (a) Variation of site-resolved order parameter Δ_i with V_0 in a one-dimensional model. (b) Variation of band gap with V_0 . (c) Variation of energy eigenvalues of a finite chain (dotted lines). The shaded region shows the energy range spanned by a periodic chain. Vertical red and blue dashed lines show two specific values of V_0 ($V_d = 3$ and $V_e = 5$, respectively). (d) and (e) The band structure close to $k = 0$ for $V_0 = V_d$ and $V_0 = V_e$, marked with red and blue dashed lines in (c). The horizontal black lines show the energy level of a finite system. (f) and (g) The probability density of the highest occupied (ψ_1) and lowest unoccupied (ψ_2) states, marked with orange and green arrows in (d) and (e), respectively. L denotes the length in units of the unit cell, and the gray regions denote the potentials.

essentially behaves like an Su-Schrieffer-Heeger model [42], where the variation of the hopping parameter can be achieved with the scalar potential. This indicates that one can tune the *mass* of the system with a scalar potential which, in turn, can influence the topology of the system. This connection will be clearer in the next section, where we discuss two-dimensional systems.

B. Tuning the topological phase in two dimensions: Emergence of the quantized Hall effect

The extension of Hamiltonian H_1 [Eq. (4)] to two dimensions is quite straightforward and is given by

$$H_2(k_x, k_y) = \{M - 2B[\cos(k_x) + \cos(k_y)]\}\sigma_3 + 2A[\sin(k_x)\sigma_1 + \sin(k_y)\sigma_2]. \quad (6)$$

One can easily recognize that this is the 2×2 block of the Hamiltonian used to define the quantum spin Hall effect in HgTe-CdTe quantum wells, commonly known as the Bernevig-Hughes-Zhang (BHZ) model [11]. The Creutz lattice [Eq. (3)] and the BHZ model [Eq. (6)] are the simplest models of a Chern insulator. In the following sections, we use the BHZ model, which exhibits a Chern number $\mathcal{C} = \text{sgn}(M)$ for $|M| < |4B|$ and $\mathcal{C} = 0$ for $|M| > |4B|$. This lends us a perfect playground for further predictions. We start with $M = 9$, $B = 2$, and $A = 5$, which gives a trivial Chern insulator state ($\mathcal{C} = 0$). The mass gap at $k_x, k_y = 0$ is given by $M - 4B$, which for our choice of parameters is 1. Here we consider a 3×3 supercell with one scalar potential (resulting in 11.1% coverage) and calculate the variation of the band structure, mass term, and Chern number (Fig. 4) with the variation of

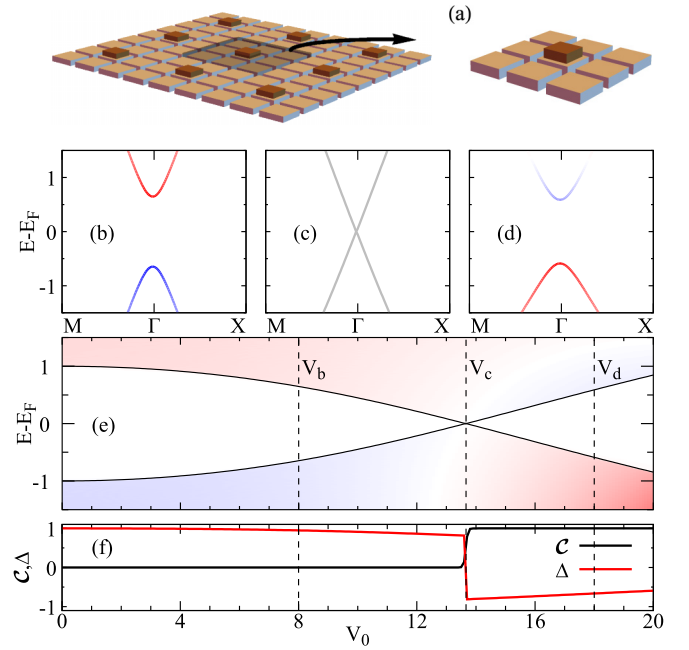


FIG. 4. Variation of the topological nature with V_0 . (a) Schematic of the supercell lattice with a 3×3 motif. Dark brown blocks correspond to areas with an additional scalar potential. (b)–(d) The band structures for $V_0 = V_b, V_c, V_d$, respectively [shown by the vertical dashed lines in (e)], with red (blue) showing positive (negative) values of $\langle \sigma_3 \rangle$. (e) The variation of the band gap with V_0 , where red (blue) corresponds to the positive (negative) value of $m(E)$. (f) The variation of the Chern number (black) and the total order parameter Δ (red) with V_0 .

V_0 . The Chern number can be calculated from

$$\mathcal{C} = \frac{1}{2\pi} \sum_n^{n_F} \int_{BZ} dk_x dk_y [f(E_n) - f(E_m)] \times \sum_{m \neq n} 2 \text{Im} \left[\frac{\langle m | \partial H / \partial k_y | n \rangle \langle n | \partial H / \partial k_x | m \rangle}{(E_n - E_m)^2} \right], \quad (7)$$

where n_F is the number of states below the Fermi level. $f(E_n)$ is the Fermi-Dirac distribution for the n th energy eigenvalue and $|n\rangle$ is the n th eigenstate. The mass term at any particular energy is given by

$$m(E) = \int_{BZ} dk_x dk_y \sum_n^{2N} \langle n | \sigma_3 \otimes \mathbb{I}_N | n \rangle \delta(E_n - E), \quad (8)$$

where N is the number of sites (which for our case is 9) and \mathbb{I}_N is the identity matrix of rank N . $\delta(x)$ is the Dirac delta function, which is approximated as a Lorentzian with broadening η , which we choose to be 0.005. For a better comparison, we use the same broadening in the calculation of the Chern number as well. Here we use the integrated order parameter, defined as

$$\Delta = [(\langle + | \sigma_3 \otimes \mathbb{I}_N | + \rangle - \langle - | \sigma_3 \otimes \mathbb{I}_N | - \rangle) / 2]_{k=0}, \quad (9)$$

which is sufficient to denote the phase transition.

With these definitions, one can clearly see the connection between the band inversion and the *mass* (Fig. 4) in two

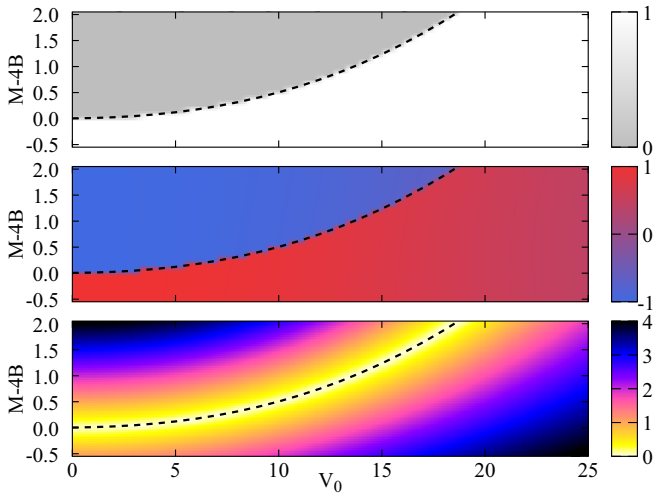


FIG. 5. Variation of (a) the Chern number C , (b) order parameter Δ , and (c) mass gap with the parameter M and the strength of the scalar potential V_0 . The black dashed line shows the transition boundary.

dimensions as well. From Fig. 4, one can see that with the increase of the scalar potential, there are a band gap closing and reopening, similar to what we observe in the one-dimensional case (Figs. 1 and 3). At the critical point, where the bands touch each other, the order parameter and the Chern number undergo a jump, indicating a change in the topological phase. This is consistent with our earlier picture of band inversion through the mixing of different mass regimes. The nonzero Chern number indicates the generation of a Hall current due to the scalar potential. Since the effect is triggered by a scalar term rather than a vector field, we call it the *scalar Hall effect*. This is to distinguish its origin. In spirit it is an emergent quantum anomalous Hall effect caused by the mixture of quantum states mediated by the scalar potential. In a topologically trivial regime, each occupied band comprises states with the same sign for the mass term. As we increase the potential, the interchange of states with opposite mass terms takes place. An increase of the scalar potential enhances the mixing of states with opposite mass terms and thus transports the system from a topologically trivial to a nontrivial phase, characterized by a nonzero Chern number. The critical potential (V_C in Fig. 4) at which the transition takes place shows a parabolic dependence with respect to the parameter M that controls the *mass* of the system (Fig. 5) and a logarithmic behavior with respect to the potential concentration (Fig. 6).

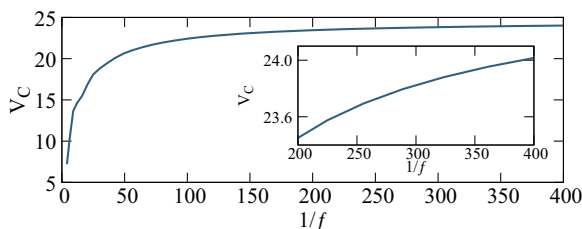


FIG. 6. Variation of the critical potential V_C with the density of the scalar potential f .

There is an important difference between the underlying mechanism leading to the scalar Hall effect and that leading to a topological Anderson insulator [43]. Theory on the Anderson insulator shows that the topological phase is formed by the dissipative state, whereas the scalar Hall effect is caused by plane waves mediated through (inverse) Klein tunneling. While the topological Anderson phase is observed within the initial metallic regime, the scalar Hall effect emerges in the gapped region. In contrast to a random disorder-induced Chern insulator [44], this mechanism is intrinsic in nature. This is reflected in the fact that the emergent nontrivial phase possesses the same magnitude of the gap as the potential-free case, whereas the disorder-induced nontrivial phase is known to have an order of magnitude smaller gap [44]. The underlying mechanism is also distinct from the previously reported mechanism for the voltage-modulated Chern number [45], in which one can arbitrarily enhance the Chern number by increasing the voltage. Our mechanism, on the other hand, facilitates a transition from $C = 0$ to $C = 1$, which is the highest Chern number possible for this model. If one starts from a topologically nontrivial configuration, the additional scalar potential enhances the topological protection and reduces the mixing of quantum states and thus prevents any further topological transition (Fig. 5).

IV. FORMATION AND MANIPULATION OF EDGE STATES

A nonvanishing bulk topological invariant has direct correspondence with the existence of edge states [46,47]. To demonstrate that, we consider a ribbon configuration; i.e., we assume a periodic boundary condition along the x direction and an open boundary condition along the y direction by repeating the block shown in Fig. 4(a). Here we choose 3 sites along x and 90 sites along y (a total of 270 sites, Fig. 7) and introduce a scalar potential V_0 in one in every nine (3×3) sites (11.1% coverage).

In such a ribbon the edge states emerge when V_0 crosses the critical value at which the bulk bands cross each other (Fig. 7). This is similar to the emergence of edge localization in a one-dimensional system (Fig. 4). Each edge hosts a single edge state such that opposite edges host states with opposite group velocities, which is expected in the case of a Chern insulator with a Chern number of 1.

One can further manipulate the behavior of the edge states locally by controlling the distribution of the scalar potential. As we explained before, the scalar potential enhances the mixing between states with opposite mass terms, which causes the topological transition. In an extended system, one can use the scalar potential selectively in different regions of space to infuse the topological nature selectively. To demonstrate this we consider the aforementioned ribbon (Fig. 7). Then we start removing the scalar potential from one end and calculate the band structure (Fig. 8). The Fermi level E_F is defined as the middle of 270th and 271th eigenvalues at the Γ point.

With this simple procedure, one can easily manipulate the edge states selectively. By removing the scalar potential at one edge, we reduce the mixing of the states locally, and as a result, the states which were sharply localized at the edges before now start moving more into the central region. This

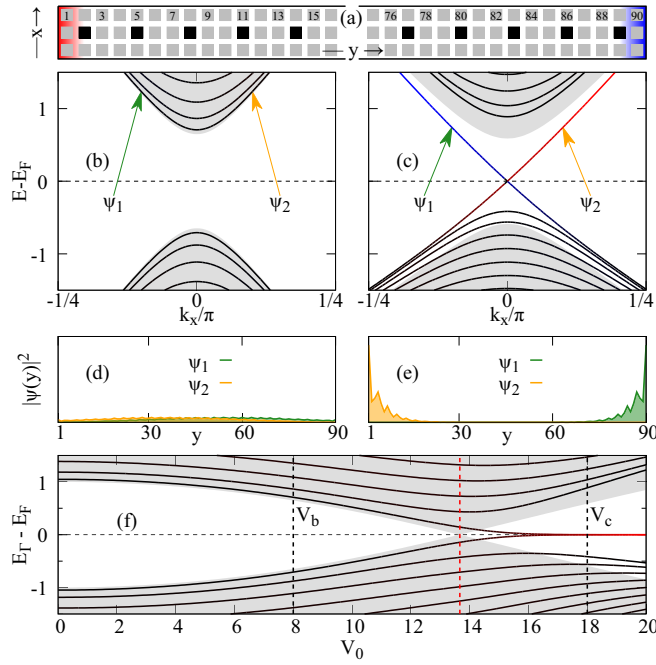


FIG. 7. Variation of bulk and edge properties with V_0 . (a) The schematic of the ribbon with scalar potentials is denoted in black. (b) and (c) The band structure for $V_0 = V_b$ and $V_0 = V_c$ [V_b and V_d in Fig. 4(e)]. Red, blue, and black mark the contributions from the edge at $y = 1$, the edge at $y = 90$, and the bulk region. Gray shaded regions mark the regions spanned by the bulk bands. (d) and (e) The probability density of states $\Psi_{1,2}$, marked with green and orange arrows in (a) and (b). (f) The variation of eigenvalues at the Γ point, where black and red correspond to the contributions from the bulk and edges. The gray regions show the areas spanned by the bulk bands, and the vertical red dashed line shows the point of band inversion [$V_0 = V_c$ in Figs. 4(c), 4(e) and 4(f)].

is manifested by the fact that the sharp red line in Fig. 8 remains intact as long as there are scalar potentials at the corresponding edges, whereas the blue lines fade out and mix strongly with the gray bands.

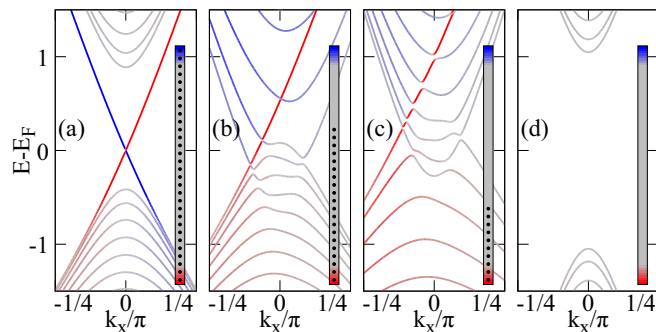


FIG. 8. Variation of the band structure with the distribution of the scalar potential along the ribbon. (a) The band structure when the full width of the ribbon is covered with the potential. (b) and (c) The band structure with 2/3 and 1/3 coverage and (d) the band structure with no potential. The inset in each plot shows the spatial distribution, where the black dots represent the scalar potential. Red and blue denote the $y = 1$ and $y = 90$ edges [Fig. 7(a)].

V. CONCLUSIONS

In this paper, we presented an alternative paradigm to infuse nontrivial topological characteristics into a trivial insulator using a scalar potential. The scalar potential was utilized to enhance the mixing between different quantum states, which in turn drives the system into a topologically nontrivial regime accompanied by a reversal in *mass* term. This switching is present in both one and two dimensions. In one dimension, it produces strong edge localization, whereas in two dimensions it shows the appearance of the chiral edge states with specific group velocity. In two dimensions, it gives rise to an emergent Hall effect which can be verified by calculating the Chern number. In addition, our method also allows us to control the topological properties by local means, which is not possible with a conventional topological insulator. We demonstrated that the edge states can be controlled by selective placement of the scalar potential. One can observe the same qualitative behavior with periodic and nonperiodic distributions of the scalar potential as long as it does not form clusters. These predictions can be realized in real materials available experimentally. A suitable candidate for such a study would be a CdTe-HgTe-CdTe quantum well, in which the topological phases can be controlled by changing the width of the well. The scalar potential can be designed with suitable fabrication techniques [48,49] or can be introduced via a nonmagnetic dopant. For a $\text{Hg}_{0.32}\text{Cd}_{0.68}\text{Te}$ -HgTe quantum well, the mass gap ($2m$) is ~ 50 meV for a thickness of 50 \AA [11], which indicates the scalar potential induced topological transition can be observed for $V_0 \lesssim 0.5$ eV. Our results thus open several new possibilities to control the topological properties and design highly controllable devices for topological electronics.

ACKNOWLEDGMENTS

S.G. would like to acknowledge helpful discussions with E. Prodan. We also gratefully acknowledge financial support by the Deutsche Forschungsgemeinschaft (DFG, German Research Foundation) – TRR 288/2 – 422213477 (project B06), TRR 173/2 – 268565370 (Project A11), CRC 1238 – 277146847 (Project C01), and the Jülich Supercomputing Centre for providing computational resources under the project jiff40.

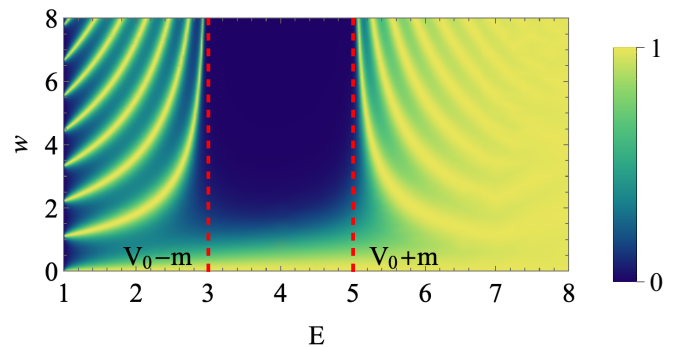


FIG. 9. Variation of the transmission probability for different energies and barrier widths in the case of a rectangular barrier introduced in a one-dimensional Dirac Hamiltonian. Here we choose $V_0 = 4$ and $m = 1$.

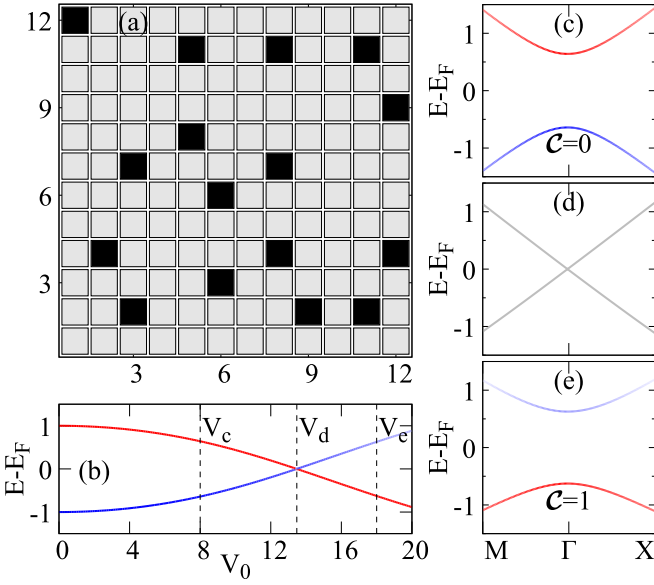


FIG. 10. Variation of the mass gap and Chern number for a supercell. (a) Distribution of the potential (black blocks) over the supercell. (b) Variation of the band gap, where red and blue lines denote positive and negative values of $\langle \sigma_z \rangle$. (c)–(e) Band structures and Chern numbers for the three different values of V_0 denoted by the vertical dashed lines in (b).

APPENDIX A: TRANSMISSION OF A MASSIVE DIRAC PARTICLE IN ONE DIMENSION THROUGH A RECTANGULAR BARRIER

Here we briefly show the transmission of a massive Dirac particle through a scalar potential, which can provide a better understanding of the modulation of the mass term. We start with a massive Dirac equation in one dimension, given by

$$H_1^D = -i\sigma_1\partial_x + \sigma_3m + \sigma_0V(x), \quad (\text{A1})$$

where m is the mass term, which we choose to be 1. $\sigma_{1,3}$ are the Pauli matrices, and σ_0 is the identity matrix of rank 2. The simplest way to study the impact of a scalar potential is to introduce a rectangular barrier of width w , such that $V(x) = V_0$ for $-w/2 \leq x \leq w/2$ and $V(x) = 0$ otherwise. The transmission probability for such a rectangular barrier is given by $T = 16|\lambda|/[(1+\lambda)^2e^{-i\kappa_2w} - (1-\lambda)^2e^{i\kappa_2w}]^2$, where $\kappa_1 = \sqrt{E^2 - m^2}$, $\kappa_2 = \sqrt{(E - V_0)^2 - m^2}$, and $\lambda = \frac{\kappa_2}{\kappa_1} \frac{E+m}{E-V_0+m}$. For such a system, it is possible to achieve complete transmission probability if the barrier height is greater than twice the mass term ($V_0 > 2m$), which manifests as multiple transmission channels for $E < V_0$ in Fig. 9.

For $w \rightarrow \infty$, the *Klein window* ($m \leq E \leq V_0 - m$) can manifest complete transmission. At this limit, the region inside and outside the scalar potential is dominated by a particular sign of the mass term. For small w , there is more mixing between the states with a different mass term, which manifests as a modulation of the transmission probability with respect to the energy on both sides of the forbidden zone ($V_0 - m \leq E \leq V_0 + m$). In a periodic lattice with a

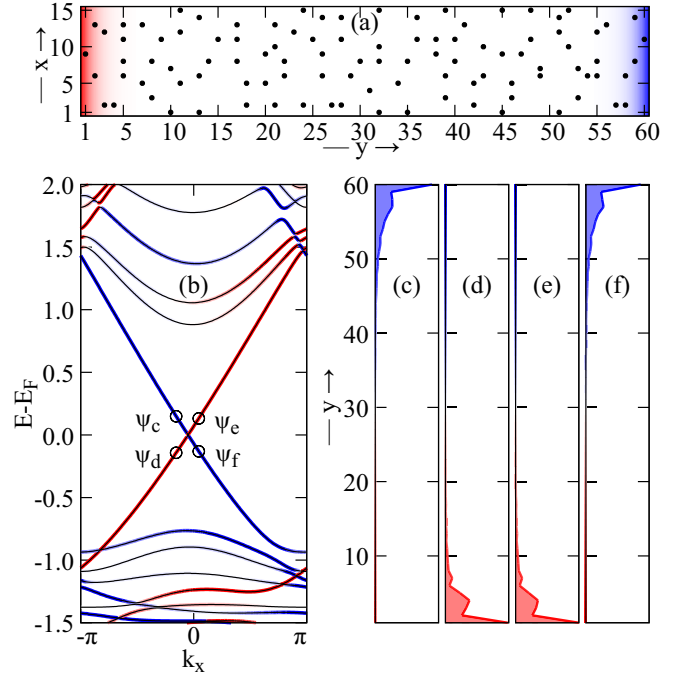


FIG. 11. Edge state formation for the extended ribbon. (a) Distribution of the potential over the ribbon. (b) The band structure of the ribbon, where red and blue lines show the contributions from the $y = 1$ and $y = 60$ edges. (c)–(f) The average probability density along the x axis for the four different states marked in (b).

fixed width of the potential region, this interference results in a modulation of the mass gap with respect to the barrier height V_0 .

APPENDIX B: RANDOM ORIENTATION OF POTENTIAL

The obvious question that arises at this point is whether this topological transition is an artifact of a perfect periodic system or not. To answer that we consider a 12×12 supercell with 16 scalar potentials (11.1% coverage) and calculate the variation of the mass gap (Fig. 10). Since calculating the Chern number for such a large system is computationally quite demanding, we calculate it for two different topological phases. One can readily see that the mass gap and the topological features change in a way similar to the small and uniform supercell (Fig. 4), which establishes that it is an intrinsic property and does not depend on the distribution of the scalar potential. Similar behavior can be observed with a ribbon with an open boundary condition along the y direction (Fig. 11). We choose a supercell of 15×60 sites and scatter 100 scalar potential with $V_0 = 20$. Here we also observe a pair of chiral edge states similar to the case of uniform distribution (Fig. 7). Note that there is a small asymmetry in the bulk states which comes from the asymmetric distribution of the scalar potential. However, it does not affect the presence of the edge states. These results confirm that the topological transition can be achieved with the scalar potential for any arbitrary distribution.

- [1] S. Ghosh, P. Rüßmann, Y. Mokrousov, F. Freimuth, and A. Kosma, Perspective on spin-orbit torque, topology, and reciprocal and real-space spin textures in magnetic materials and heterostructures, *J. Appl. Phys.* **133**, 230901 (2023).
- [2] O. Breunig and Y. Ando, Opportunities in topological insulator devices, *Nat. Rev. Phys.* **4**, 184 (2021).
- [3] M. J. Gilbert, Topological electronics, *Commun. Phys.* **4**, 70 (2021).
- [4] S.-Y. Lin, M. Chen, X.-B. Yang, Y.-J. Zhao, S.-C. Wu, C. Felser, and B. Yan, Theoretical search for half-Heusler topological insulators, *Phys. Rev. B* **91**, 094107 (2015).
- [5] Y. Ando, Topological insulator materials, *J. Phys. Soc. Jpn.* **82**, 102001 (2013).
- [6] A. Altland and M. R. Zirnbauer, Nonstandard symmetry classes in mesoscopic normal-superconducting hybrid structures, *Phys. Rev. B* **55**, 1142 (1997).
- [7] S. Ryu, A. P. Schnyder, A. Furusaki, and A. W. W. Ludwig, Topological insulators and superconductors: Tenfold way and dimensional hierarchy, *New J. Phys.* **12**, 065010 (2010).
- [8] N. P. Armitage, E. J. Mele, and A. Vishwanath, Weyl and Dirac semimetals in three-dimensional solids, *Rev. Mod. Phys.* **90**, 015001 (2018).
- [9] B.Q. Lv, T. Qian, and H. Ding, Experimental perspective on three-dimensional topological semimetals, *Rev. Mod. Phys.* **93**, 025002 (2021).
- [10] K. v. Klitzing, G. Dorda, and M. Pepper, New method for high-accuracy determination of the fine-structure constant based on quantized Hall resistance, *Phys. Rev. Lett.* **45**, 494 (1980).
- [11] B. A. Bernevig, T. L. Hughes, and S.-C. Zhang, Quantum spin Hall effect and topological phase transition in HgTe quantum wells, *Science* **314**, 1757 (2006).
- [12] H. Zhang, C.-X. Liu, X.-L. Qi, X. Dai, Z. Fang, and S.-C. Zhang, Topological insulators in Bi₂Se₃, Bi₂Te₃ and Sb₂Te₃ with a single Dirac cone on the surface, *Nat. Phys.* **5**, 438 (2009).
- [13] N. Nagaosa, J. Sinova, S. Onoda, A. H. MacDonald, and N. P. Ong, Anomalous Hall effect, *Rev. Mod. Phys.* **82**, 1539 (2010).
- [14] J. Sinova, S. O. Valenzuela, J. Wunderlich, C. H. Back, and T. Jungwirth, Spin Hall effects, *Rev. Mod. Phys.* **87**, 1213 (2015).
- [15] S. Murakami, N. Nagaosa, and S.-C. Zhang, Dissipationless quantum spin current at room temperature, *Science* **301**, 1348 (2003).
- [16] T. Fukazawa, H. Kohno, and J. Fujimoto, Intrinsic and extrinsic spin Hall effects of Dirac electrons, *J. Phys. Soc. Jpn.* **86**, 094704 (2017).
- [17] A. Crépieux and P. Bruno, Theory of the anomalous Hall effect from the Kubo formula and the Dirac equation, *Phys. Rev. B* **64**, 014416 (2001).
- [18] J. H. Cullen and D. Culcer, Spin-Hall effect due to the bulk states of topological insulators: Extrinsic contribution to the proper spin current, *Phys. Rev. B* **108**, 245418 (2023).
- [19] D. J. Thouless, M. Kohmoto, M. P. Nightingale, and M. den Nijs, Quantized Hall conductance in a two-dimensional periodic potential, *Phys. Rev. Lett.* **49**, 405 (1982).
- [20] S. Ghosh, S. Blügel, and Y. Mokrousov, Ultrafast optical generation of antiferromagnetic meron-antimeron pairs with conservation of topological charge, *Phys. Rev. Res.* **5**, L022007 (2023).
- [21] S. Ghosh and A. Manchon, Spin-orbit torque in two-dimensional antiferromagnetic topological insulators, *Phys. Rev. B* **95**, 035422 (2017).
- [22] E. Cheng, W. Xia, X. Shi, H. Fang, C. Wang, C. Xi, S. Xu, D. C. Peets, L. Wang, H. Su, L. Pi, W. Ren, X. Wang, N. Yu, Y. Chen, W. Zhao, Z. Liu, Y. Guo, and S. Li, Magnetism-induced topological transition in EuAs₃, *Nat. Commun.* **12**, 6970 (2021).
- [23] S. Shamim, W. Beugeling, P. Shekhar, K. Bendias, L. Lunczer, J. Kleinlein, H. Buhmann, and L. W. Molenkamp, Quantized spin Hall conductance in a magnetically doped two dimensional topological insulator, *Nat. Commun.* **12**, 3193 (2021).
- [24] Z. Zhu, Y. Cheng, and U. Schwingenschlögl, Band inversion mechanism in topological insulators: A guideline for materials design, *Phys. Rev. B* **85**, 235401 (2012).
- [25] F. D. M. Haldane, Model for a quantum Hall effect without Landau levels: Condensed-matter realization of the “parity anomaly,” *Phys. Rev. Lett.* **61**, 2015 (1988).
- [26] L. Fu, Topological crystalline insulators, *Phys. Rev. Lett.* **106**, 106802 (2011).
- [27] R. Jackiw and C. Rebbi, Solitons with fermion number $\frac{1}{2}$, *Phys. Rev. D* **13**, 3398 (1976).
- [28] D. Xiao, M.-C. Chang, and Q. Niu, Berry phase effects on electronic properties, *Rev. Mod. Phys.* **82**, 1959 (2010).
- [29] S. Ghosh and A. Manchon, Nonequilibrium spin density and spin-orbit torque in a three-dimensional topological insulator/antiferromagnet heterostructure, *Phys. Rev. B* **100**, 014412 (2019).
- [30] S. Ghosh and A. Manchon, Signature of topological phases in zitterbewegung, *SPIN* **6**, 1640004 (2016).
- [31] C. L. Kane and E. J. Mele, Z₂ topological order and the quantum spin Hall effect, *Phys. Rev. Lett.* **95**, 146802 (2005); Quantum spin Hall effect in graphene, **95**, 226801 (2005).
- [32] H.-N. Barad, H. Kwon, M. Alarcón-Correa, and P. Fischer, Large area patterning of nanoparticles and nanostructures: Current status and future prospects, *ACS Nano* **15**, 5861 (2021).
- [33] L. Esaki and R. Tsu, Superlattice and negative differential conductivity in semiconductors, *IBM J. Res. Dev.* **14**, 61 (1970).
- [34] O. Klein, Die reflexion von elektronen an einem potentialsprung nach der relativistischen dynamik von Dirac, *Z. Phys.* **53**, 157 (1929).
- [35] M. I. Katsnelson, K. S. Novoselov, and A. K. Geim, Chiral tunnelling and the Klein paradox in graphene, *Nat. Phys.* **2**, 620 (2006).
- [36] B. H. J. McKellar and G. J. Stephenson, Relativistic quarks in one-dimensional periodic structures, *Phys. Rev. C* **35**, 2262 (1987).
- [37] S. Ghosh and A. Saha, Persistent current of relativistic electrons on a Dirac ring in presence of impurities, *Eur. Phys. J. B* **87**, 167 (2014).
- [38] In the continuum limit, a filled Dirac sea contains an infinite number of particles, and the notion of Fermi level is not well defined.
- [39] H. B. Nielsen and M. Ninomiya, A no-go theorem for regularizing chiral fermions, *Phys. Lett. B* **105**, 219 (1981).
- [40] K. G. Wilson, Confinement of quarks, *Phys. Rev. D* **10**, 2445 (1974).
- [41] M. Creutz and I. Horváth, Surface states and chiral symmetry on the lattice, *Phys. Rev. D* **50**, 2297 (1994).
- [42] W. P. Su, J. R. Schrieffer, and A. J. Heeger, Solitons in polyacetylene, *Phys. Rev. Lett.* **42**, 1698 (1979).

- [43] C. W. Groth, M. Wimmer, A. R. Akhmerov, J. Tworzydło, and C. W. J. Beenakker, Theory of the topological anderson insulator, *Phys. Rev. Lett.* **103**, 196805 (2009); J. Li, R.-L. Chu, J. K. Jain, and S.-Q. Shen, Topological Anderson insulator, *ibid.* **102**, 136806 (2009).
- [44] Y. Kuno, Disorder-induced Chern insulator in the Harper-Hofstadter-Hatsugai model, *Phys. Rev. B* **100**, 054108 (2019).
- [45] Z.-F. Jiang, R.-L. Chu, and S.-Q. Shen, Electric-field modulation of the number of helical edge states in thin-film semiconductors, *Phys. Rev. B* **81**, 115322 (2010).
- [46] Y. Hatsugai, Chern number and edge states in the integer quantum Hall effect, *Phys. Rev. Lett.* **71**, 3697 (1993).
- [47] X.-L. Qi, Y.-S. Wu, and S.-C. Zhang, General theorem relating the bulk topological number to edge states in two-dimensional insulators, *Phys. Rev. B* **74**, 045125 (2006).
- [48] J. Caro, E. W. J. M. van der Drift, K. L. Hagemans, and S. Radelaar, Fabrication of grating gates for lateral surface superlattice devices using E-beam lithography, *Microelectron. Eng.* **5**, 273 (1986).
- [49] D. Q. Wang, D. Reuter, A. D. Wieck, A. R. Hamilton, and O. Klochan, Two-dimensional lateral surface superlattices in GaAs heterostructures with independent control of carrier density and modulation potential, *Appl. Phys. Lett.* **117**, 032102 (2020).